OPEN

Correspondence and
requests for materials
should be addressed to
M.-Y.C. (mychou6@
gate.sinica.edu.tw) or
L.-J.L. (lanceli@gate.
sinica.edu.tw)

Ultrahigh-Gain Photodetectors Based on Atomically Thin Graphene-MoS$_2$ Heterostructures

Wenjing Zhang[1], Chih-Piao Chuu[1], Jing-Kai Huang[1,2], Chang-Hsiao Chen[1], Meng-Lin Tsai[3], Yung-Huang Chang[1], Chi-Te Liang[4], Yu-Ze Chen[5], Yu-Lun Chueh[5], Jr-Hau He[3], Mei-Yin Chou[1,4,6] & Lain-Jong Li[1,7,8]

[1]Institute of Atomic and Molecular Sciences, Academia Sinica, Taipei, 11529, Taiwan, [2]Department of Photonics, National Chiao Tung University, HsinChu 300, Taiwan, [3]Graduate Institute of Photonics and Optoelectronics, and Department of ElectricalEngineering, National Taiwan University, Taipei, Taiwan, [4]Department of Physics, National Taiwan University, Taipei, Taiwan, [5]Department of Materials Science and Engineering, National Tsing-Hua University, Hsinchu, 300, Taiwan, [6]School of Physics, Georgia Institute of Technology, Atlanta, GA 30332, USA, [7]Department of Physics, National Tsing Hua University, HsinChu 300, Taiwan, [8]Department of Medical Research, China Medical University Hospital, Taichung, Taiwan.

Due to its high carrier mobility, broadband absorption, and fast response time, the semi-metallic graphene is attractive for optoelectronics. Another two-dimensional semiconducting material molybdenum disulfide (MoS$_2$) is also known as light- sensitive. Here we show that a large-area and continuous MoS$_2$ monolayer is achievable using a CVD method and graphene is transferable onto MoS$_2$. We demonstrate that a photodetector based on the graphene/MoS$_2$ heterostructure is able to provide a high photogain greater than 10^8. Our experiments show that the electron-hole pairs are produced in the MoS$_2$ layer after light absorption and subsequently separated across the layers. Contradictory to the expectation based on the conventional built-in electric field model for metal-semiconductor contacts, photoelectrons are injected into the graphene layer rather than trapped in MoS$_2$ due to the presence of a perpendicular effective electric field caused by the combination of the built-in electric field, the applied electrostatic field, and charged impurities or adsorbates, resulting in a tuneable photoresponsivity.

Two-dimensional (2d) nanomaterials, such as graphene and MoS$_2$, hold great promise in next-generation electronic and photonic applications because of their unique properties inherited from the ultrathin planar structures, such as strong electron-hole confinement, extreme bendability, and high transparency, which allow for the fabrication of thinner, more flexible and more efficient devices[1,2]. Graphene has attracted substantial attention in optoelectronic applications due to its high carrier mobility, broad absorption spectrum, and fast response time. Graphene can absorb light and turn it into a photocurrent, and a recent study has shown that graphene serves as an excellent light-to-current converter with a quantum efficiency reaching close to 100% owing to its long mean-free path and high Fermi velocity[3]. However, graphene absorbs only 2.3% of light in the wide range of visible spectra[4]. Although various approaches such as graphene plasmons[5,6], microcavities[7,8] and metallic plasmons[9] have been employed to enhance light absorption in graphene, the photogain of graphene-based photodetectors still has more room to improve. The photoresponse mechanisms in various types of graphene-based devices have been identified, including the photovoltaic effect[10–15], the thermoelectric Seebeck effect[15–19] and the bolometric effect[20]. Although the fast recombination of photoexcited carriers in graphene may not be advantageous for photoresponsivity, the high carrier mobility in graphene offers a great possibility to show high photoresponsivity if a proper graphene device structure is built[21,22].

Assembling graphene with various 2d layers into artificial heterostructures to demonstrate new or tailored properties has been proposed[23] and realized in tunneling field-effect transistors[24–26] very recently. The photo-response efficiency of graphene devices, in principle, can be greatly enhanced by exploiting a vertical geometry, for instance, graphene/2d semiconductor heterostructural stacking, where the whole graphene area can be used as a junction. The layered MoS$_2$ is a newly emerging 2d nanomaterial with a direct and finite band gap. Recent reports have demonstrated a gigantic photoluminescence (PL) from the MoS$_2$ monolayer, 4-fold higher than that in its bulk, owing to the quantum confinement effect associated with the transition from an indirect band gap in

the bulk to a direct band gap in the monolayer[27–33]. The photodetectors based on MoS_2 thin layers have shown reasonably high photoresponsivity in ambient ranging from 7.5 mA/W to 780 A/W[34–36]. Very recently, the graphene/WS_2/graphene heterostructural device with a WS_2 thickness of 5–50 nm has also been demonstrated to exhibit a photoresponsivity ~0.1 A/W[37]. In this work, we fabricate a photodetector based on a graphene-on-MoS_2 heterostructure, where the MoS_2 monolayer grown by chemical vapor deposition (CVD) is used to absorb light and produce electron-hole pairs. The photo-excited electron-hole pairs are separated at the MoS_2 and graphene interfaces, where the electrons move to graphene due to the presence of a perpendicular effective electric field created by the combination of the built-in electric field, the applied electrostatic field, and charged impurities or adsorbates. The photodetector based on the graphene/MoS_2 heterostructure is able to reach a photoresponsivity value higher than 10^7 A/W and a photogain of about 10^8 at room temperature.

Results

Preparation of stacking layers. In our previous work[38], we have reported the direct growth of MoS_2 monolayer crystal flakes on a sapphire or SiO_2 substrate by the vapour-phase reaction of MoO_3 and S powders in a hot-wall chemical vapour deposition (CVD) system. Here we report that this method can be further extended to grow on SiO_2 a continuous MoS_2 layer composed of randomly oriented crystalline MoS_2 domains with an average domain size around several microns. High purity MoO_3 (0.3 g; from Aldrich; 99% purity) was placed in a ceramic boat at the heating center of the furnace. A SiO_2/Si Substrate was placed in the downstream side adjacent to the ceramic boat. Sulfur powder was heated by heating tape (160°C) and carried by Ar (Ar = 70 sccm at 10 torr) to the furnace heating center. The furnace was gradually heated from room temperature to 650°C with a rate of 25°C/min. After keeping at 250°C for 10 minutes, the furnace was naturally cooled down to room temperature. The experimental set-up for the growth is shown in the supporting Figure S1. The as-grown MoS_2 was mostly monolayer although we also noticed that the growth of small-sized second layer of MoS_2 was initiated at the center of some monolayer domains. Large-area monolayer graphene was grown on copper foils at 1000°C by a CVD method using a mixture of methane and hydrogen gases as reported elsewhere[39,40]. To stack the graphene monolayer on MoS_2, a layer of PMMA thin film was coated on the graphene/Cu foil as a transfer supporting layer[41,42]. After the wet etching of Cu by an aqueous solution containing Fe^{3+} ions, the PMMA-supported graphene film was transferred to the top of the as-grown MoS_2 film, followed by the removal of PMMA using acetone. The photograph in Figure 1a is the top view of the graphene/MoS_2 heterostructure simply formed by a manual stacking of a large-area CVD graphene monolayer onto MoS_2.

Spectroscopic charaterizations. In Figure 1a, monolayer MoS_2 film was directly grown on the right hand side of the SiO_2/Si wafer followed by the transfer of graphene to the bottom half; therefore, we can see a clear difference in the optical contrast at four quadrants. Figure 1b schematically illustrates the device structure adopted in the study, where the top view of the comb-shaped source and drain metals is also shown below. We have performed the TEM cross-section study for the graphene/MoS_2 device. Figure 1c shows the TEM cross-section view, where the graphene/MoS_2 is capped with a passivation layer of SiO_2, and the intensity profile on the right hand side shows that the thicknesses of graphene and MoS_2 are as expected, 0.36 nm and 0.7 nm. There is no PMMA residue in between graphene and MoS_2 layers. Figure 1d displays the Raman spectrum
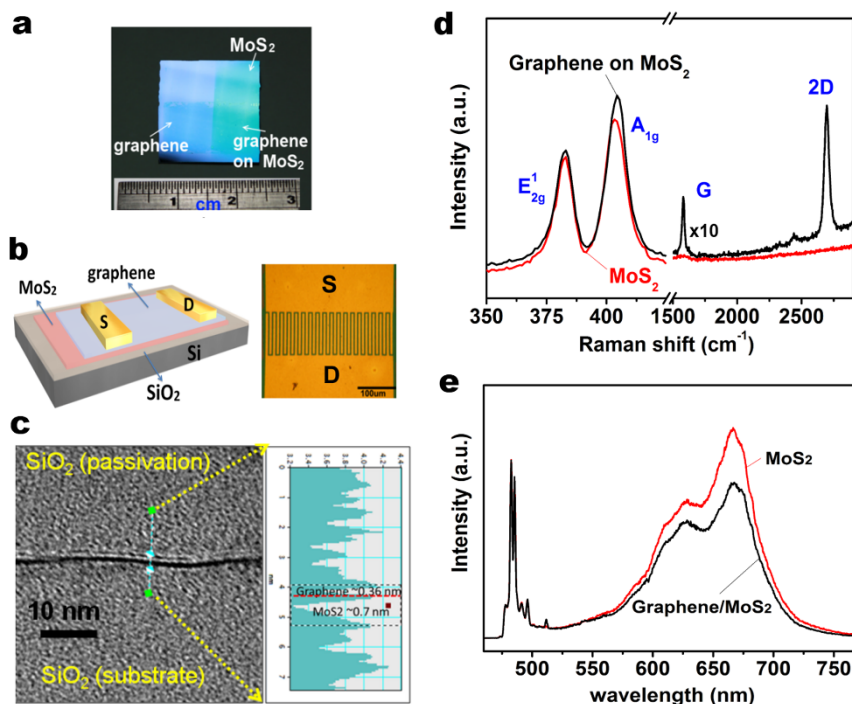

Figure 1 | Spectroscopic characterizations of a graphene/MoS_2 bilayer. (a) Photo showing that a MoS_2 monolayer was grown on the right hand side of the 300 nm SiO_2/Si wafer followed by transferring graphene onto the bottom half. (b) Schematic illustration of the photodetector based on graphene/MoS_2 stacked layers, where the channel is formed in between the comb-shaped source and drain metal electrodes (Ti/Au = 5 nm/80 nm). (c) A high-resolution TEM (HRTEM) image clearly reveals a bilayer stacking of graphene/MoS_2. The thickness of each layer can be extracted from the intensity profile to be 0.36 nm and 0.7 nm for graphene and MoS_2, respectively. (d) Raman spectra and (e) photoluminescence spectra for MoS_2 and MoS_2 covered by CVD monolayer graphene taken from the sample shown in (a). Note that the Raman intensity of Graphene/MoS_2 in (d) has been multiplied by a factor of 10 for better comparison.

of the MoS_2 monolayer on SiO_2/Si and that of MoS_2 covered by graphene, taken from the sample shown in Figure 1a. The energy difference between the Raman E^1_{2g} and A_{1g} peaks is ~19.0 cm^{-1}, indicating that the MoS_2 film is monolayer[28–30]. The optical micrograph of a MoS_2 film on a SiO_2 substrate is shown in supporting Figure S2a. The Raman mapping in supporting Figure S2b shows that the distribution of the energy difference between the Raman E^1_{2g} and A_{1g} peaks is uniform across the sample. The AFM cross-sectional height shown in supporting Figures S2c and S2d confirms that the film is monolayer. The peaks at about 2695.9 cm^{-1} and 1581.5 cm^{-1} are the characteristics of 2D and G bands, respectively for monolayer graphene[39]. Figure 1e illustrates that the photoluminescence (PL) spectrum for MoS_2 covered by graphene (graphene/MoS_2) maintains a similar shape as its pristine form (without graphene on top) except that the intensity is decreased.

Photoelectron movement. Before discussing the photocurrent behavior, we examine the carrier properties when graphene contacts with MoS_2 in dark. First, we obtain the carrier concentrations and resistances of the graphene and graphene/MoS_2 sheets on SiO_2 by the Hall-effect measurements in dark at room temperature. All the samples are the same size (0.5 cm × 0.5 cm), and each sample has been measured four times. Since MoS_2 is much less conductive compared with graphene, the carrier properties obtained are mainly from graphene. Note that significant numbers of reports have shown that CVD graphene is *p*-doped in ambient caused by the doping effect from transfer process, adsorbed moisture/oxygen and the substrate impurities[43,44]. Supporting Figures S3a and S3b demonstrate that the hole concentration in graphene decreases from 6×10^{12} cm^{-2} to 2×10^{12} cm^{-2} and the resistance significantly increases when graphene is in contact with MoS_2, suggesting that electrons possibly move from MoS_2 to graphene. Second, we prepared the graphene and graphene/MoS_2 transistors on a SiO_2/Si substrate with the same device fabrication processes. The electrical transfer curves in supporting Figure S3c demonstrate that the charge neutral point (V_{CNP}) of the graphene/MoS_2 transistor shifted to the left compared with that of a graphene transistor, indicating that the graphene/MoS_2 transistor was less hole-doped, consistent with the conclusion from Hall-effect measurements.

The Raman spectra in Figure 2a show that the G band of monolayer graphene on SiO_2/Si is at 1585.4 cm^{-1} and it is broadened with a downshift to 1581.7 cm^{-1} when a MoS_2 layer is present underneath at room temperature. Since the increase in G band peak width could be related to the increase in disorder or other reasons, both the changes in G band peak width and position should be used in order to characterize the doping in graphene. Note that the integrated intensity of D band for the graphene on SiO_2/Si is not significantly different from that on MoS_2 (Figure S4). Therefore, we do not have evidence to show that the G band broadening is attributed to the increase in disorder. Because the graphene transferred by PMMA is known as *p*-doped, the red shift and broadening of the G band indicate that the Fermi level of graphene is raised (or an increase in the electron concentration) with the light exposure[45]. These results suggest that the photoelectrons generated by the Raman laser are injected into graphene. The Raman mappings of the G band energy and the FWHM are also shown to consolidate the conclusion. To further reveal the effect of adding graphene on MoS_2, Raman features for MoS_2 with and without graphene coverage are examined. The Raman spectra and mappings in Figure 2b show that the A_{1g} peak is up-shifted by ~1 cm^{-1} in energy and the peak width is narrowed after being covered by graphene, indicating that the MoS_2 layer becomes less *n*-doped (or a decrease in the electron concentration)[46]. Recent report has shown that the level of ~3×10^{12} cm^{-2} p-doping on MoS_2 leads to ~1 cm^{-1} of up-shift for the A_{1g} peak[46], where we can estimate the photogenerated holes by Raman laser is in the order of 10^{12} cm^{-2}. For comparison, we have also fabricated a stacking
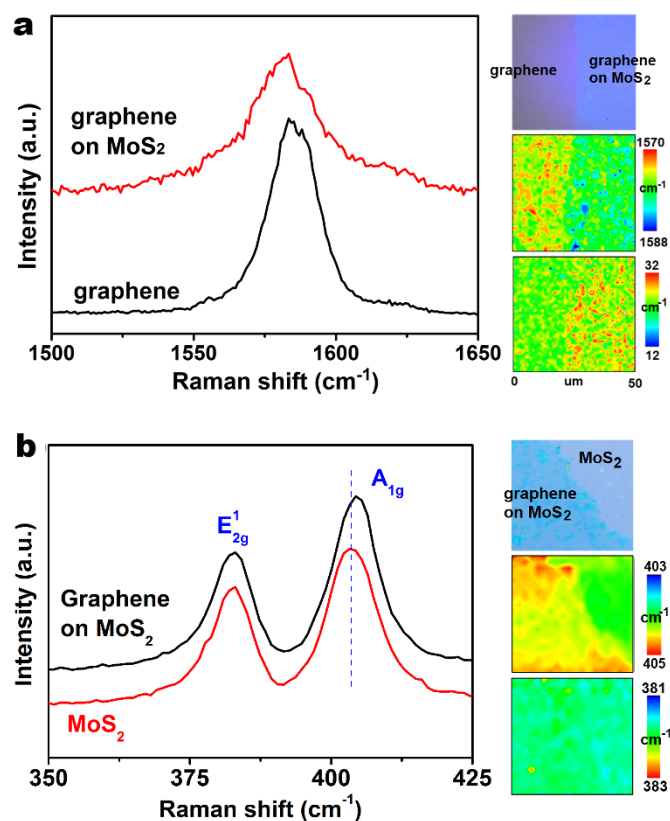
Figure 2 | Raman characterizations. (a) Raman mappings and representative Raman spectra for graphene and graphene on MoS_2, where the G band energy of graphene on SiO_2 is higher than that transferred on MoS_2. (b) Raman mappings and representative Raman spectra for MoS_2 and that covered with graphene. The A_{1g} energy of MoS_2 is up-shifted when graphene is transferred onto it, suggesting that the electron density in MoS_2 is lowered (with electrons moving from MoS_2 to graphene). The excitation source is a 473-nm laser.

structure MoS_2/graphene by transferring MoS_2 monolayer onto a *p*-typed graphene layer on SiO_2 substrates at room temperature. The Raman spectra and mappings shown in supporting Figure S5 demonstrate that when the MoS_2/graphene stack is exposed to light, the graphene layer also receives electrons from MoS_2. Both structures consistently show that the photo-excited electrons move from MoS_2 to graphene, and the photo-excited holes are trapped in the MoS_2 layer.

High photoresponsivity and photgain. To quantify the photocarriers, we study the dependence of the photocurrent on light power for the graphene/MoS_2 transistor at room temperature. Figure 3a shows the transfer curves for the graphene/MoS_2 transistor exposed to the 650-nm light with various power densities (device structure shown in Figure 1b). The voltage of the charge neutral point V_{CNP} for the transfer curve in dark is at around 10 V, indicating that graphene is *p*-doped. The shape of the transfer curve is very similar to that for pristine graphene on SiO_2, suggesting that the carrier transport in the graphene/MoS_2 photodetector is dominated by graphene. The result is reasonable because graphene is much more conductive than the MoS_2 layer. The graphene/MoS_2 transistor is extremely sensitive to light. When light is illuminated on the graphene/MoS_2 transistor, the drain current (I_d) in the *p*-channel decreases and the I_d in the *n*-channel increases as shown in Figure 3a, indicating that the photoexcited electrons are injected into graphene. The photocurrent dependence on gate voltage is plotted in Figure 3b. At the same time, the V_{CNP} largely shifted to
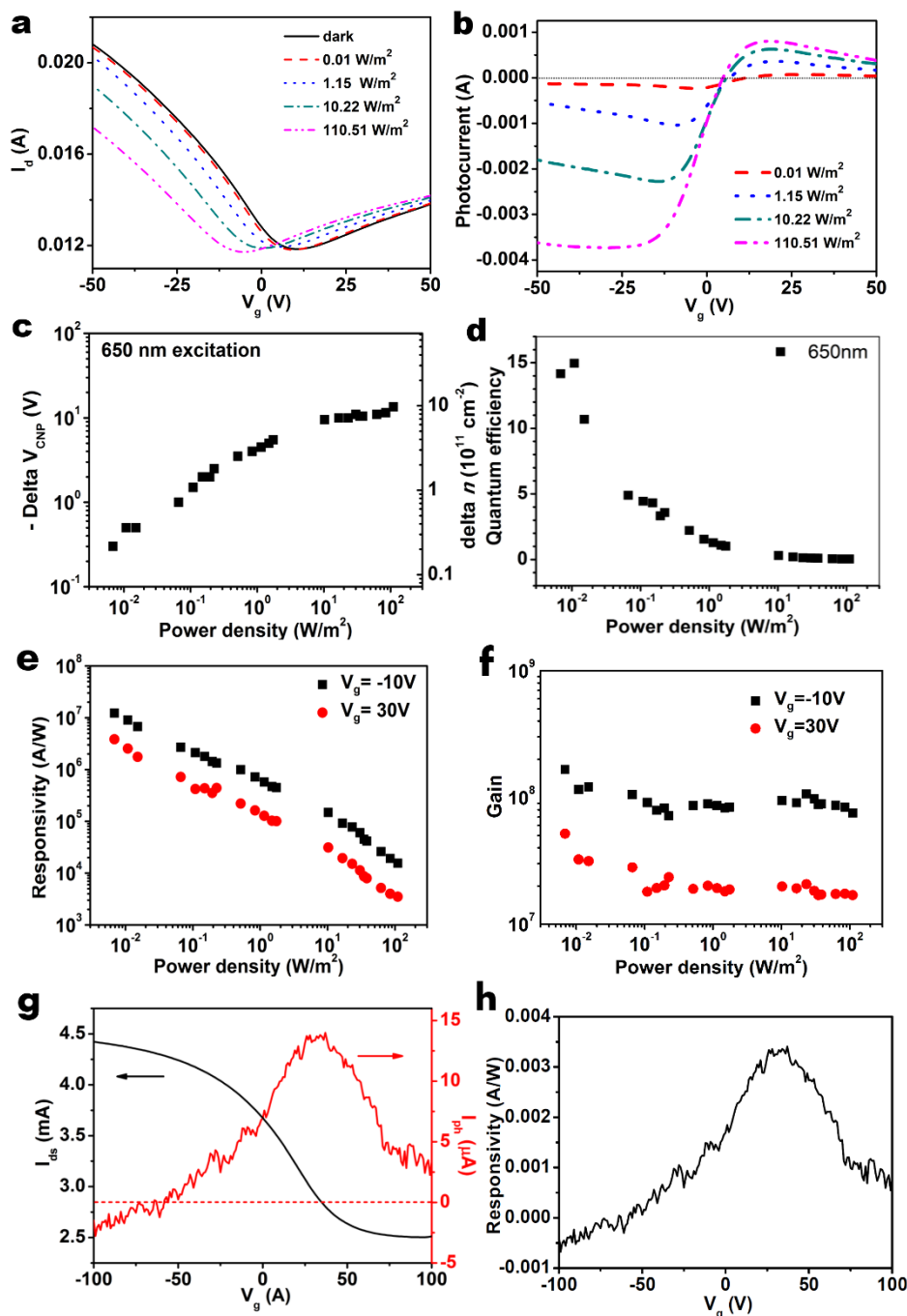
Figure 3 | Photoresponses of the graphene/MoS₂ devices. (a) Transfer curves for the graphene/MoS$_2$ photodetector s under the exposure of light with various powers. (b) Photocurrent as a function of the gate voltage based on the transfer curves obtained in (a). (c) Shift of the charge neutral point V$_{CNP}$ and the corresponding electron density change (delta n) for a graphene/MoS$_2$ photodetector with various light powers. (d) Quantum efficiency, (e) photoresponsivity and (f) photogain for the graphene/MoS$_2$ photodetectors. The wavelength of the laser is 650 nm, and the channel area for exposure is ~2.0×10^{-8} m^2. (g) Photocurrent and (h) photoresponsivity of a photodetector based on a CVD graphene layer. A continuous wavelength 532 nm laser was used to illuminate the device at power density 35.21 W/cm^2 (V$_{ds}$ = 0.1 V).

a more negative voltage even with very weak light exposure (Figure 3c). The negative shift of V$_{CNP}$ indicates that the photoexcited holes were trapped in the MoS$_2$, acting as an additional positive gate voltage for graphene[21]. The carrier concentration of the trapped holes can be extracted using the formula $\Delta n = C_g \times \Delta V_{CNP}/e$ for graphene, where $C_g = 1.15 \times 10^{-8}$ F/cm^2 for the dielectric film of 300 nm SiO$_2$, and e is the electron charge[21,45,47]. The internal quantum efficiency (IQE), a measurement of a photodetector's electrical sensitivity to light, can be estimated by the equation: IQE = (the number of photoexcited

electron-hole pairs)/(absorbed number of photons) = $\Delta n \times$ A/(P$_o$/ $h\nu$), where A, P$_o$, h and ν represent the total channel area, absorbed light power by graphene and MoS$_2$, the Planck constant and the frequency of the incident laser, respectively. (Note that the absorbance of the graphene/MoS$_2$ heterostructure is ~6.8% at 650 nm based on our absorption measurement.) As shown in Figure 3d, the IQE decreases with the increasing light power and the largest IQE for the system is ~15%. We further estimate the photoresponsivity and photogain to quantify the photo sensitivity of the graphene/MoS$_2$ photodetector. The photoresponsivity is the

ratio between the photocurrent ($I_{ph} = I_{light} - I_{dark}$) and the light power absorbed by the photodetector, and, remarkably, the photoresponsivity can reach 1.2×10^7 A/W (at $V_g = -10$ V; $V_{ds} = 1$ V; light power density ~ 0.01 W/m²) as shown in Figure 3e. The photogain can be calculated by the formula $G = I_{ph}/[e \times$ (the number of photoexcited electron-hole pairs)] $= I_{ph}/(e \times \Delta n \times A)$, and the gain is up to 10^8 (Figure 3f).

In our device structure, the metals only contact to the top layer graphene, not the MoS₂ layer. Meanwhile, as described in text, the measured current is actually dominated by graphene. Hence, it is also crucial to examine whether the CVD graphene itself contributes to the observed large photocurrent. Our measured results in Figures 3g and 3h (and in supporting Figure S6) are consistent with those reported by Avouris' group[15] in that the intrinsic photoresponse in biased graphene transistors was dominated by the photovoltaic effect and a photoinduced bolometric effect, while the thermoelectric effect was insignificant. However, the photocurrent generated from the pure graphene transistors is several orders of magnitude smaller than that observed in our graphene/MoS₂ photodetector, indicating that the observed large photocurrent from graphene/MoS₂ is not contributed by the aforementioned processes in graphene. On the other hand, we fabricated the CVD monolayer MoS₂ photodetector in the same device configuration, and found that the highest photoresponsivity for the pristine monolayer MoS₂ is around 780 A/W[36] In the present experiment, the graphene-based photodetector with an ultrahigh photo sensitivity $\sim 10^7$ A/W is realized simply by stacking it onto an atomically thin MoS₂ layer.

Discussion

In addition to the move of photoelectrons to graphene, the negative shift of V_{CNP} upon photoexcitation may also be attributed to other extrinsic effects such as thermal desorption of absorbed dopants or thermoelectric effect. Figure 4a shows the dependence of photoresponsivity of the graphene/MoS₂ transistor on the wavelength of light at room temperature. It is observed that photoresponsivity only becomes pronounced when the excitation energy is higher than the absorption band gap of MoS₂ (1.8 eV)[32], with the optical absorption feature of the as-grown MoS₂ layer shown in Figure 4b. These results suggest that the photocurrent is originated from the light absorption in MoS₂: the electron-hole pairs are produced in MoS₂, followed by the separation of them between MoS₂ and graphene layers. If the photocurrent were from the thermal effect, the photocurrent would have been induced even when the photon energy is smaller than the band gap of monolayer MoS₂.

To further exclude the thermal effect, we measured the time-resolved photocurrent driven by different drain voltages at a low laser power density at room temperature, which ensures that the fast current self-heating effect becomes more prominent for the thermal desorption process or thermoelectric effect. Detailed results of time-resolved photoresponse and arguments were presented in the supporting Figure S7 to show that the photocurrent of the graphene/MoS₂ photodetector is not from the thermal effects. In brief, the normalized photocurrent-time profiles for the graphene/MoS₂ transistor in ambient air shown in Figure S7a reveals that the current-time curve obtained at $V_{ds} = 0.002$ V overlaps with that at $V_{ds} = 0.01$ V. The photocurrent becomes smaller when V_{ds} is set at 1 V (current I_{ds} is $\sim 2 \times 10^{-2}$ A). If the thermal desorption of dopants or thermoelectric effect from the film was a dominant process, a higher V_{ds} would have given rise to a larger photocurrent[48]. The measurement results in vacuum also consistently lead to the same conclusion that thermal effect is not a dominant process.

After monolayer graphene and monolayer MoS₂ contact with each other, the electrons are injected into graphene. Thus, the conventional theory of ideal metal-semiconductor contacts predicts an energy-band bending at the interface as shown in supporting Figure S8, and the direction of the built-in electric field is from
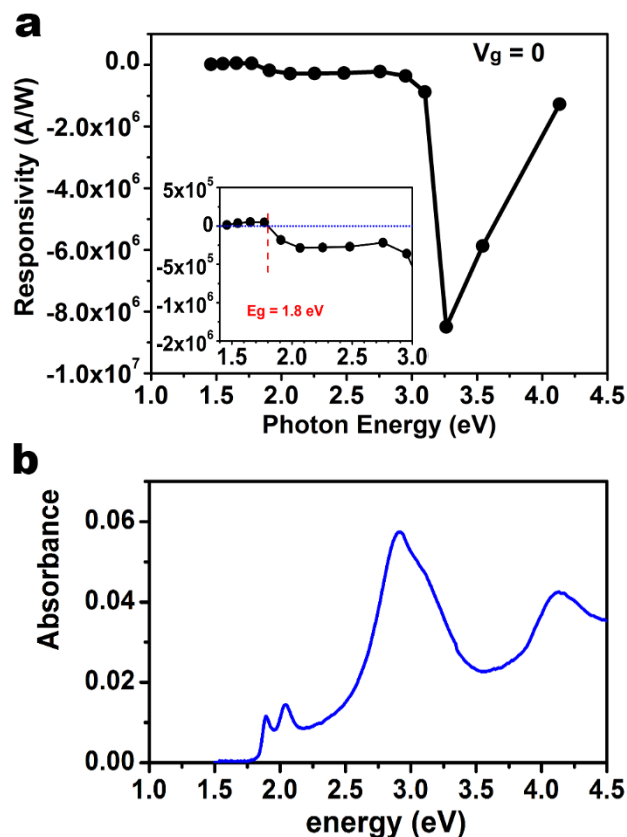
Figure 4 | Wavelength dependence. (a) Photoresponsivity as a function of the energy of the excitation light source. (b) Optical absorption spectrum for monolayer MoS₂.

MoS₂ to graphene. With illumination on the graphene/MoS₂ transistors, the photo-generated electrons should flow into MoS₂. However, this is opposite to our experimental results. Different from the conventional metal-semiconductor contact, the semimetal and semiconductor of the 2d heterostructure are atomically thin layers, and the depletion region of the 2d heterostructure is so thin that the charge concentration and polarity at the interface of graphene/MoS₂ should be liable to be affected by the charge impurities on the surfaces of graphene and MoS₂ or the applied electrostatic field. The applied electric field and the external electric field that is from the charge impurities on the surface of graphene and MoS₂ form an effective electric field at the graphene/MoS₂ interface. The effective electric field determines the flowing direction and the amount of the photoexcited electrons. As mentioned above in Figure 2 and Figure S5, the MoS₂ donates electrons to graphene for both the structures of graphene/MoS₂ and MoS₂/graphene, indicating that the direction of the effective electric field of the 2d heterostructure in ambient air is from graphene to MoS₂. When the sample is in high vacuum ($\sim 5 \times 10^{-5}$ mbarr), the graphene accepts electrons when shining light on the devices as presented in Figure 5, which means that the direction of the effective electric field is still from graphene to MoS₂. However, the photocurrent is much smaller than that in ambient air at the same laser power density, suggesting that the effective electric field decreases in high vacuum. As shown in Figure 5a, the V_{CNP} of the second device shifted to the left by ~ 23 V, indicating that the many adsorbates or charged impurities are desorbed in high vacuum, and the graphene reverts it polarity from p- to n-type. Our previous result has shown that the monolayer MoS₂ film still remains n-doped in high vacuum[36]. Thus it is intuitive to derive that the effective electric field at the graphene/MoS₂ interface in air is larger than that in vacuum.
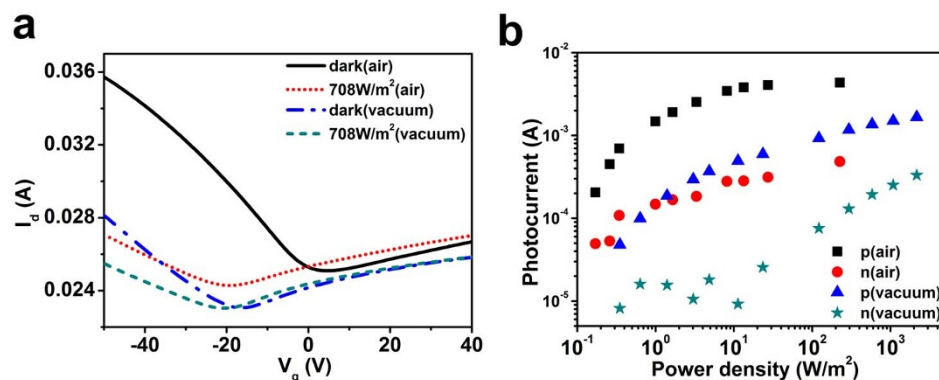
Figure 5 | Comparison of photoresponses in air and in vacuum. (a) Transfer curves for the graphene/MoS$_2$ transistor measured in air and in vacuum. (b) Photocurrent as a function of the light power density in air and in vacuum at $V_g - V_{CNP} = \pm 20$ V. The 532-nm laser was used to measure the photocurrent, and the spot size was $\sim$2 mm.

To exploit the alignment of the Fermi level between the heterostructure, first-principles calculations are performed based on density functional theory (DFT)[49,50] using the Vienna *ab initio* simulation package (VASP)[51,52]. The details are described in Methods. A modulated electric field (E_{ext}) is applied to simulate the doping effect and align the energy bands in graphene/MoS$_2$. The band structure corresponding to the bilayer in air is shown in Figure 6a with *p*-doped graphene and *n*-doped MoS$_2$. After pumping that removes *p*-dopants, the band structure of the bilayer in vacuum is shown in Figure 6b with *n*-doped graphene and *n*-doped MoS$_2$. The corresponding schematic illustration of the photoelectron

transfer process is also shown in Figure 6. From the Figure 6, we can find that the effective electric field of the p-doped graphene/MoS$_2$ heterostructure would be larger than that of the *n*-doped graphene, so the photogenerated electron-hole pairs would be separated more easily by this effective electric field. The more *n*-doped graphene, the smaller effective electric field, and leading to the smaller photogain. So the photoresponsivity of the graphene/MoS$_2$ photodetector can be tuned by the modulation of the doping level of graphene and MoS$_2$. As the monolayer MoS$_2$ has a band gap $\sim$1.8 eV, and the graphene is semimetal, the photoresponsivity is more sensitive to the graphene doping level.
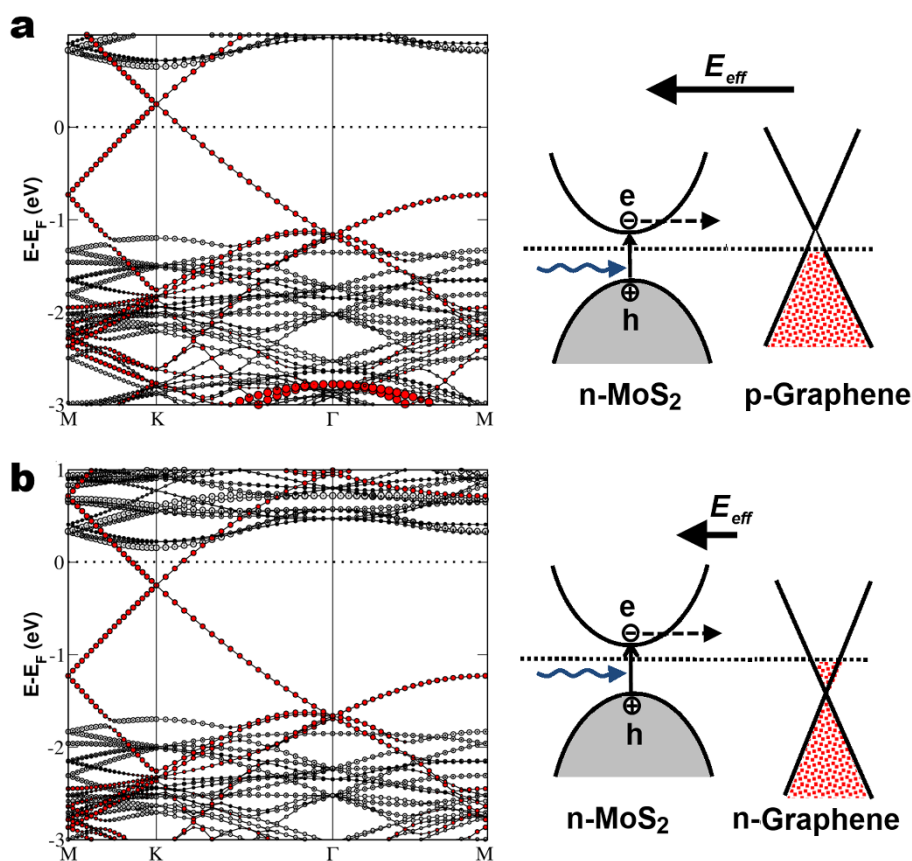
Figure 6 | Schematic illustration of the photoelectron transfer process in the graphene/MoS$_2$ bilayer. The corresponding band structures for an *n*-doped MoS$_2$ layer topped with (a) slightly *p*-doped graphene and (b) *n*-doped graphene corresponding to the experimental situation in air and in vacuum, respectively. The electronic states associated with graphene and MoS$_2$ are represented in red and gray in the band structure plots, respectively. The effective electric field is created by charged impurities or adsorbated (see text).

The high photogain process in the graphene/MoS_2 bilayer can now be described as follows. Light absorption in MoS_2 generates electron-hole pairs; the electrons can move to the graphene layer due to an effective electric field created by the combination of the built-in electric field, the applied electrostatic field, and charged impurities or adsorbates, while the holes are trapped in the MoS_2 layer. It is noted that the V_{th} shift is a direct result of electron transfer from MoS_2 to graphene. In addition to the electron-hole separation, the high electron mobility in graphene and the long charge-trapping lifetime of the holes result in multiple recirculation of electrons in graphene, leading to a very high photogain. This high-photogain mechanism is similar to what was reported by Yan and Konstantatos et al. for bilayer graphene where a thick layer of PbS quantum dots was used as the light absorber[21], although the controlling scheme for charge separation there is intrinsically different from that in the current heterostructure formed by 2d layered materials. It is noted that the graphene/MoS_2 stacking is with a high photogain but not a high on/off photocurrent ratio since the graphene layer is intrinsically with a low on/off current. To achieve a better on/off switching ratio in the stacking structure, graphene nanoribbens or gapped graphene may be used in the future.

Conclusions

In conclusion, we have constructed a graphene/MoS_2 bilayer by manually stacking graphene on a CVD MoS_2 layer. The advantage of using this structure for photodetection is that the whole surface area can be used as a junction, where electron–hole pairs can be separated at the interface. The photodetector based on this graphene/MoS_2 heterostructure is able to reach a photoresponsivity value higher than 10^7 A/W while maintaining its unique ultrathin character. The present work demonstrates the significance of charge movement in the emerging field of 2d heterostructures. The heterostructures of 2d layers exhibit novel materials properties beyond the capacities of the constituents. Stimulations of research and developments of optoelectronic applications based on various heterostructural 2d materials are thus anticipated.

Methods

Characterizations. The AFM images were performed in a Veeco Dimension-Icon system. Raman and photoluminescence (PL) spectra were collected in a confocal Raman/PL system (NT-MDT). The wavelength of laser is 473 nm (2.63 eV), and the spot size of the laser beam is ~0.5 μm. The step size of the Raman spatial mapping is 0.5 μm, and the spectral resolution is 3 cm^{-1} (obtained with a 600 grooves/mm grating). A high grating (1800 grooves/mm) is also used to get more details of the line shapes of the Raman band, and the spectral resolution is 1 cm^{-1}. The Si peak at 520 cm^{-1} was used as a reference for wavenumber calibration, and the peak frequency was extracted by fitting a Raman peak with a Lorentz function. The electrical measurements were performed in an ambient or vacuum condition using a Keithley semiconductor parameter analyzer, model 4200-SCS. The sheet resistance, sheet concentration, and mobility of the graphene and graphene on MoS_2 films were analyzed by using a Hall sensor measurement based on the Van der Pauw method[53]. Field-emission transmission electron microscopy (JEM-3000 F, JEOL operated at 300 kV with point-to-point resolution of 0.17 nm) equipped with an energy dispersion spectrometer (EDS) was used to obtain the microstructures and the chemical compositions. The sample for TEM measurements was prepared by a focus ion beam (FIB) (SMI 3050SE, SII Nanotechnology). Before sample cutting, the sample was capped by a 100 nm-thick SiO_2 layer deposited by an E-gun system as a passivation layer in order to prevent the damage from Ga ions during sample cutting.

Numerical simulation. We construct a slab model with a 5×5 supercell of graphene on a 4×4 supercell of MoS_2 to simulate the stacked layer, where the interactions between electrons and ions is described by the projector augmented wave (PAW) method, and the exchange-correlation potential is described by the local density approximation (LDA). The lattice constant of graphene used in the simulation is 2.46 Å. The lattice constant for optimized monolayer MoS_2 is 3.12 Å. A vacuum thickness of 15 Å is used in order to eliminate the spurious image interactions, and the energy cut-off of plane waves is 400 eV. The interlayer spacing between MoS_2 and graphene is 3.3 Å for the optimized structure. An applied electric filed is added to simulate the effects of an applied gate voltage or Coulomb impurities. The calculated band gap of MoS_2 is 1.8 eV, which is known to be underestimated by LDA.

1. Novoselov, K. S. et al. A roadmap for graphene. Nature 490, 192–200 (2012).
2. Wang, Q. H. et al. Electronics and optoelectronics of two-dimensional transition metal dichalcogenides. Nature Nanotechnol. 7, 699–712 (2012).
3. Mueller, T., Xia, F. & Avouris, P. Graphene photodetectors for high-speed optical communications. Nature Photon. 4, 297–301 (2010).
4. Nair, R. R. et al. Fine structure constant defines visual transparency of graphene. Science 320, 1308–1308 (2010).
5. Koppens, F. H. L., Chang, D. E. & García de Abajo, F. J. Graphene plasmonics: a platform for strong light–matter interactions. Nano Lett. 11, 3370–3377 (2011).
6. Thongrattanasiri, S., Koppens, F. H. L. & Garcia de Abajo, F. J. Complete optical absorption in periodically patterned graphene. Phys. Rev. Lett. 108, 047401–047405 (2012).
7. Furchi, M. et al. Microcavity-integrated graphene photodetector. Nano Lett. 12, 2773–2777 (2012).
8. Engel, M. et al. Light–matter interaction in a microcavity-controlled graphene transistor. Nature Commun. 3, 906; DOI: 10.1038/ncomms1911 (2012).
9. Echtermeyer, T. J. et al. Strong plasmonic enhancement of photovoltage in graphene. Nature Commun. 2, 458; DOI:10.1038/ncomms1464 (2011).
10. Lee, E. J. H., Balasubramanian, K., Weitz, R. T., Burghard, M. & Kern, K. Contact and edge effects in graphene devices. Nature Nanotechnol. 3, 486–490 (2008).
11. Mueller, T., Xia, F., Freitag, M., Tsang, J. & Avouris, P. Role of contacts in graphene transistors: A scanning photocurrent study. Phys. Rev. B 79, 245430–245436 (2009).
12. Xia, F. et al. Photocurrent imaging and efficient photon detection in a graphene transistor. Nano Lett. 9, 1039–1044 (2009).
13. Peters, E. C., Lee, E. J., Burghard, M. & Kern, K. Gate dependent photocurrents at a graphene p-n junction. Appl. Phys. Lett. 97, 193102–193104 (2010).
14. Rao, G., Freitag, M., Chiu, H.-Y., Sundaram, R. S. & Avouris, P. Raman and Photocurrent Imaging of electrical stress-induced p-n junctions in graphene. ACS Nano 5, 5848–5854 (2011).
15. Freitag, M. et al. Photoconductivity of biased graphene. Nature Photon. 7, 53–59 (2013).
16. Xu, X., Gabor, N. M., Alden, J. S., Van der Zande, A. M. & McEuen, P. L. Photo-thermoelectric effect at a graphene interface junction. Nano Lett. 10, 562–566 (2009).
17. Lemme, M. C. et al. Gate-activated photoresponse in a graphene p-n junction. Nano Lett. 11, 4134–4137 (2011).
18. Song, J. C. W., Rudner, M. S., Marcus, C. M. & Levitov, L. S. Hot carrier transport and photocurrent response in graphene. Nano Lett. 11, 4688–4692 (2011).
19. Gabor, N. M. et al. Hot Carrier-assisted intrinsic photoresponse in graphene. Science 334, 648–652 (2011).
20. Yan, J. et al. Dual-gated bilayer graphene hot electron bolometer. Nature Nanotechnol. 7, 427–478 (2012).
21. Konstantatos, G. et al. Hybrid graphene–quantum dot phototransistors with ultrahigh gain. Nature Nanotechnol. 7, 363–368 (2012).
22. Sun, Z. et al. Infrared photodetectors based on CVD-grown graphene and PbS quantum dots with ultrahigh reponsivity. Adv. Mater. 24, 5878–5883 (2012).
23. Novoselov, K. S. & Neto, A. H. Castro Two-dimensional crystals-based heterostructures: materials with tailored properties. Phys. Scr. T146, 014006 (2012).
24. Dean, C. et al. Graphene based heterostructures. Solid State Commun. 152, 1275–1282 (2012).
25. Britnell, L. et al. Field-effect tunneling transistor based on vertical graphene heterostructures. Science 24, 947–950 (2012).
26. Yu, W. J. et al. Vertically stacked multi-heterostructures of layered materials for logic transistors and complementary inverters. Nature Mater. 12, 246–252 (2013).
27. Radisavljevic, B., Radenovic, A., Brivio, J., Giacometti, V. & Kis, A. Single-layer MoS₂ transistors. Nature Nanotechnol. 6, 147–150 (2011).
28. Zhang, Y., Ye, J., Matcuhashi, Y. & Iwasa, Y. Ambipolar MoS₂ thin flake transistors. Nano Lett. 12, 1136–1140 (2012).
29. Liu, K. K. et al. Growth of large-area and highly crystalline MoS₂ thin layers on insulating substrates. Nano Lett. 12, 1538–1544 (2012).
30. Lin, Y.-C. et al. Wafer-scale MoS₂ thin layers prepared by MoO₃ sulfurization. Nanoscale 4, 6637–6641 (2012).
31. Eda, G. et al. Photoluminescence from chemically exfoliated MoS₂. Nano Lett. 11, 5111–5116 (2011).
32. Mak, K. F., Lee, C., Hone, J., Shan, J. & Heinz, T. F. Atomically thin MoS₂: a new direct-gap semiconductor. Phys. Rev. lett. 105, 136805–136808 (2010).
33. Zeng, H., Dai, J., Yao, W., Xiao, D. & Cui, X. Valley polarization in MoS₂ monolayers by optical pumping. Nature Nanotechnol. 7, 490–493 (2012).
34. Yin, Z. et al. Single-layer MoS₂ phototransistors. ACS Nano 6, 74–80 (2012).
35. Tsai, D. S. et al. Few-Layer MoS2 with High Broadband Photogain and Fast Optical Switching for Use in Harsh Environments. ACS Nano; DOI: 10.1021/nn305301b (2013).
36. Zhang, W. J. et al. High-Gain Phototransistors Based on a CVD MoS₂ Monolayer. Adv. Mater. 25, 3456–3461 (2013).
37. Britnell, L. et al. Strong Light-Matter Interactions in Heterostructures of Atomically Thin Films. Science 340, 1311–1314 (2013).
38. Lee, Y.-H. et al. Synthesis of large-area MoS₂ atomic layers with chemical vapor deposition. Adv. Mater. 24, 2320–2325 (2012).
39. Lu, A.-Y. et al. Decoupling of CVD graphene by controlled oxidation of recrystallized Cu. RSC Adv. 2, 3008–3013 (2012).
40. Chen, C.-H. et al. Electrical probing of submicroliter liquid using graphene strip transistors built on a nanopipette. Small 8, 43–46 (2012).

41. Hsu, C.-L. *et al.* Layer-by-layer graphene/TCNQ stacked films as conducting anodes for organic solar cells. *ACS Nano* **6**, 5031–5039 (2012).

42. Su, C.-Y. *et al.* Direct formation of wafer scale graphene thin layers on insulating substrates by chemical vapor deposition. *Nano Lett.* **11**, 3612–3616 (2011).

43. Zhang, W. J. *et al.* Opening an electrical band gap of bilayer graphene with molecular doping. *ACS Nano* **5**, 7517–7524 (2011).

44. Ryu, S. *et al.* Atmospheric oxygen binding and hole doping in deformed graphene on a SiO_2 substrate. *Nano Lett.* **10**, 4944–4951 (2010).

45. Das, A. *et al.* Monitoring dopants by Raman scattering in an electrochemically top-gated graphene transistor. *Nature Nanotechnol.* **3**, 210–215 (2008).

46. Chakraborty, B. *et al.* Symmetry-dependent phonon renormalization in monolayer MoS_2 transistor. *Phys. Rev. B* **85**, 161403(R) (2012).

47. Zhang, W. J. *et al.* The screening of charged impurities in bilayer Graphene. *New J. of Phys.* **12**, 103037 (2010).

48. Prades, J. D. *et al.* The effects of electron–hole separation on the photoconductivity of individual metal oxide nanowires. *Nanotechnol.* **19**, 465501 (2008).

49. Hohenberg, P. & Kohn, W. Inhomogeneous electron gas. *Phys. Rev.* **136**, B864–B871 (1964).

50. Leenaerts, O., Partoens1, B. & Peeters, F. M. Water on graphene: Hydrophobicity and dipole moment using density functional theory. *Phys. Rev. B* **79**, 235440–235444 (2009).

51. Kresse, G. & Furthmuller, J. Efficiency of *ab-initio* total energy calculations for metals and semiconductors using a plane-wave basis set. *Comput. Mater. Sci.* **6**, 15–50 (1996).

52. Kresse, G. & Furthmuller, J. Efficient iterative schemes for *ab initio* total-energy calculations using a plane-wave basis set. *Phys. Rev. B* **54**, 11169–11186 (1996).

53. Lin, C.-T. *et al.* Label-free electrical detection of DNA hybridization on graphene by Hall effect measurements: revisit to the sensing mechanism. *Adv. Func. Mater.* DOI: 10.1002/adfm.201202672 (2013).

Author contributions

W.Z. performed the major part of the experiments. C.P.C. performed simulation studies. J.K.H., C.H.C. and Y.H.C. helped to grow graphene and MoS_2 samples. M.L.T., C.T.L. J.H. He provide facilities. Y.Z.C. and Y.L.C. helped on TEM measurement. All authors discussed the simulation results. L.J.L., M.Y.C. and W.Z. wrote the manuscript. Correspondence for experiments and simulation should be addressed to L.J.L. (lanceli@gate.sinica.edu.tw) and M.Y.C. (mychou6@gate.sinica.edu.tw) respectively.

Additional information

Supplementary information accompanies this paper at http://www.nature.com/scientificreports

Competing financial interests: The authors declare no competing financial interests.

How to cite this article: Zhang, W.J. *et al.* Ultrahigh-Gain Photodetectors Based on Atomically Thin Graphene-MoS2 Heterostructures. *Sci. Rep.* **4**, 3826; DOI:10.1038/srep03826 (2014).